Supporting Information

Anthraquinone-Based Electroactive Ionic Species as Stable Multi-Redox Anode Active Materials for High-Performance Nonaqueous Redox Flow Battery

Yihan Zhen[a,b], Cuijuan Zhang[*a,b], Jiashu Yuan[a,b], Yongdan Li[*a,b,c]

[a] State Key Laboratory of Chemical Engineering, Tianjin Key Laboratory of Applied Catalysis Science and Technology, School of Chemical Engineering and Technology, Tianjin University, Tianjin 300072, China. Email: cjzhang@tju.edu.cn

[b] Collaborative Innovation Center of Chemical Science and Engineering (Tianjin), Tianjin 300072, China

[c] Department of Chemical and Metallurgical Engineering, School of Chemical Engineering, Aalto University, Kemistintie 1, Espoo, P.O. Box 16100, FI-00076, Aalto, Finland. Email: yongdan.li@aalto.fi

Experimental section

1. Materials

1-aminoanthraquinone (98%), Chloroacetyl chloride (99%), Methyl iodide (99%), and (Dimethylaminomethyl) ferrocene (97%) were purchased form Adamas, China; lithium bis(tetrafluoromethylsulfonyl)amide (LiTFSI, 99.5%), Tetraethylammonium bromide (TEAB, 99%), Lithium Tetrafluoroborate (LiBF$_4$, 99%), and Lithium Hexafluorophosphate (LiPF$_6$, 99%) from Meryer, China; Ether (99.5%), Ethanol (99.5%), Ethyl acetate (99%), and benzene (99%) from Jiangtian, China; trimethylamine (40 wt. % in H$_2$O) from Energy chemical, China; DMSO (99%) and NaHCO$_3$ (99%) from HEOWS, China; acetonitrile (MeCN, 99.9%) from Aladdin, China. All the materials were used as received. The supporting electrolyte tetraethylammonium bis(trifluoromethylsulfonyl)imide (TEATFSI) was synthesized according to the literature [1].

2. Synthesis of active materials

Synthesis of *l-(chloroacetylamino)anthraquinone (AQCl)*: AQCl was synthesized by modifying the reported procedure[2] : Chloroacetyl chloride (3.3882 g, 1.5 eq) was added to a stirring suspension of 1-aminoanthraquinone (AQN, 4.4646 g, 1eq) in benzene (150 mL). The mixture was stirred at 70 °C for 2 h. The precipitate was isolated by filtration and washed sequentially with saturated NaHCO$_3$, deionized water and ethanol, respectively. The yellow product was dried under vacuum for 24 h and obtained at 5.34 g, 89% yield. 1H NMR (500 MHz, DMSO- d_6) δ 12.73 (s, 1H), 8.99 (dd, J = 8.4, 1.3 Hz, 1H), 8.30 – 8.23 (m, 1H), 8.23 – 8.15 (m, 1H), 8.02 (dd, J = 7.7, 1.3 Hz, 1H), 8.00 – 7.91 (m, 3H), 4.60 (s, 2H).

Synthesis of *acetamide, 2-(N,N,N-trimethylamino)-N-(9,10-dioxo-9,10-dihydroanthracen-1-yl)-, chloride (AQNCl)*: Adding 60 mL DMSO to AQCl (2.9970 g, 1eq) and stiring vigorously, and

then the trimethylamine (40% aqueous solution, 2.2166 g, 1.5 eq) was added. The mixture was stirred at 80 °C for 6 h. A large amount of ethyl acetate was added to the reaction mixture to precipitate the product. The precipitate was isolated by filtration and washed with ethyl acetate. The yellow product was dried under vacuum for 24 h and obtained at 3.47 g, 96% yield. ^{1}H NMR (500 MHz, DMSO-d_6) δ 12.15 (s, 1H), δ 8.78 (dd, J = 8.4, 1.3 Hz, 1H), 8.23 (ddd, J = 8.7, 6.5, 2.2 Hz, 2H), 8.09 (dd, J = 7.7, 1.3 Hz, 1H), 8.03 – 7.94 (m, 3H), 4.65 (s, 2H), 3.35 (s, 9H). HRMS (ESI) calculated for $C_{19}H_{19}N_2O_3^+$ m/z = 323.1390, found m/z = 323.1405.

Synthesis of *acetamide, 2-(N,N,N-trimethylamino)-N-(9,10-dioxo-9,10-dihydroanthracen-1-yl)-, bis(trifluoromethylsulfonyl)imide (AQNTFSI)*: LiTFSI (2.7560 g, 1.2 eq) was dissolved in 50 mL deionized water (DI-H_2O) and added to the solution of AQNCl (2.8706 g, 1 eq) in 250 mL DI-H_2O. The mixture was stirred at room temperature for 6 h. The yellow solid was filtered and washed with DI-H_2O and dried under vacuum for 24 h, giving product 3.99 g, 83% yield. ^{1}H NMR (500 MHz, DMSO-d_6) δ 12.14 (s, 1H), 8.78 (dd, *J* = 8.4, 1.2 Hz, 1H), 8.22 (ddt, *J* = 7.6, 6.1, 1.9 Hz, 2H), 8.08 (dt, *J* = 7.7, 1.5 Hz, 1H), 7.97 (ddt, *J* = 8.0, 4.6, 1.5 Hz, 3H), 4.64 (s, 2H), 3.34 (s, 9H). HRMS (ESI) calculated for $C_{19}H_{19}N_2O_3^+$ m/z = 323.1390, found m/z = 323.1398; calculated for $C_2F_6S_2O_4N^-$ m/z = 279.9167, found m/z = 279.9177.

Synthesis of *acetamide, 2-(N,N,N-trimethylamino)-N-(9,10-dioxo-9,10-dihydroanthracen-1-yl)-, tetrafluoroborate (AQNBF$_4$)*: LiBF$_4$ (0.3937 g, 1.05 eq) was dissolved in 15 mL deionized water (DI-H_2O) and added to the solution of AQNCl (1.4353 g, 1 eq) in 100 mL DI-H_2O. The mixture was stirred at room temperature for 6 h. The yellow solid was filtered and washed with DI-H_2O and dried under vacuum for 24 h, giving product 1.02g, 62% yield. ^{1}H NMR (500 MHz, DMSO-d_6) δ 12.14 (s, 1H), 8.78 (dd, *J* = 8.4, 1.2 Hz, 1H), 8.22 (ddd, *J* = 7.8, 6.1, 2.1 Hz, 2H), 8.08 (dt, *J* = 7.7, 1.3 Hz, 1H), 7.98 (ddt, *J* = 9.9, 5.6, 4.0 Hz, 3H), 4.64 (s, 2H), 3.34 (s, 9H).

HRMS (ESI) calculated for $C_{19}H_{19}N_2O_3^+$ m/z = 323.1390, found m/z = 323.1400; calculated for BF_4^- m/z = 86.0060, found m/z = 86.0068.

Synthesis of *acetamide, 2-(N,N,N-trimethylamino)-N-(9,10-dioxo-9,10-dihydroanthracen-1-yl)-, hexafluorophosphate (AQNPF$_6$)*: LiPF$_6$ (0.6380 g, 1.05 eq) was dissolved in 15 mL deionized water (DI-H$_2$O) and added to the solution of AQNCl (1.4353 g, 1 eq) in 100 mL DI-H$_2$O. The mixture was stirred at room temperature for 6 h. The yellow solid was filtered and washed with DI-H$_2$O and dried under vacuum for 24 h, giving product 1.36 g, 73% yield. ^{1}H NMR (500 MHz, DMSO-d_6) δ 12.14 (s, 1H), 8.78 (dd, J = 8.4, 1.3 Hz, 1H), 8.22 (ddd, J = 7.7, 6.2, 2.2 Hz, 2H), 8.08 (dd, J = 7.7, 1.3 Hz, 1H), 8.02 – 7.93 (m, 3H), 4.64 (s, 2H), 3.34 (s, 9H). HRMS (ESI) calculated for $C_{19}H_{19}N_2O_3^+$ m/z = 323.1390, found m/z = 323.1404; calculated for PF$_6^-$ m/z = 144.9636, found m/z = 144.9622.

Synthesis of *(Ferrocenylmethyl)trimethylammonium bis(trifluoromethanesulfonyl)imide (FcNTFSI)*: Methyl iodide (5.58 g, 1.05 eq) was added to the solution of (dimethylaminomethyl)ferrocene (9.1 g, 1 eq) in 60 mL MeCN, then the mixed solution was stirred at room temperature for 12 h. The precipitate was isolated by filtration and washed with ether and dried under vacuum for 24 h (13.15 g, 91% yield). Then, the generated product (6.0 g, 1 eq) was dissolved in 200 mL deionized water, added with LiTFSI (5.7416 g, 1.25 eq) aqueous solution, the mixture was stirred at room temperature for 4 h. The product FcNTFSI was filtered and dried under vacuum for 24 h (8.13 g, 94% yield). ^{1}H NMR (500 MHz, Chloroform-d) δ 4.42 (s, 2H), 4.37 (d, J = 4.7 Hz, 4H), 4.26 (s, 5H), 3.02 (s, 9H).

3. Characterization

Cyclic voltammetry (CV) tests: The CV tests were carried out using a three-electrode configuration at room temperature with 1 mM active materials in 0.1 M TEATFSI/MeCN

deoxygenated by bubbling with Argon (99.999%, Huanyu, China) on a VersaSTAT3 electrochemical workstation (Princeton Applied Research, USA). A glassy carbon (3 mm in diameter, Aidahengsheng, China), graphite plate (5.24 cm^2), and Ag/Ag$^+$ (0.5 M AgNO$_3$/MeCN) were employed as the working, counter, and reference electrodes, respectively. The CV tests of the electrolyte after charge/discharge cycling were conducted in argon-filled glove box (Mikrouna, China).

Linear sweep voltammetry (LSV) tests: The LSV tests were performed at a scan rate of 10 mV s^{-1} with 5 mM active materials in 0.1 M TEATFSI/MeCN with a three-electrode configuration on a CHI 660D Electrochemical Workstation (Shanghai Chenhua Instruments Co., Ltd., China). The working electrode, a glassy carbon disk electrode (5 mm Teflon encased), was polished using Al$_2$O$_3$ suspended in deionized water and then rinsed and dried before testing. The graphite plate and Ag/Ag$^+$ were employed as the counter and reference electrodes, respectively. Then, the working electrode was rotated from 400 to 2500 rpm using a modulated speed rotator (AFMSRCE 061906, PINE), and the LSV scans were recorded from -0.4 to -2.2 V and -0.4 to 1.0 V for negative and positive electrolyte, respectively.

Flow battery tests: A home-designed flow battery with serpentine flow field was examined by LAND battery test instrument (Wuhan LAND Electronic Co. Ltd., China) in argon-filled glove box. Two pieces of 2 mm thick graphite felt electrodes (4 cm^2, Beihaitansu, China) with a compression ratio of 20% were ultrasonically cleaned with ethanol and deionized water and dried under vacuum before test. The electrolytes (5 mL on each side) circulated between cells and storage tanks by two peristaltic pumps (BT100-1L, Longer Precision Pump Co., Ltd., China) at a flow rate of 30 mL min^{-1}. The polarization curves were measured through LSV at the rate of 100 mV s^{-1} after the battery was charged to certain state of charge (SOC).

Solubility and conductivity measurement: The solubility of anthraquinone-based electroactive ionic liquids was tested by Ultraviolet–visible spectroscopy (UV–Vis) absorption spectra (Perkin Elmer, Lambda 750, USA). The standard curves were measured through a range of standard solutions that prepared by dissolving active species in MeCN with different concentration, and calculated by recording the absorbance of the peak wavelengths at 353 nm. The saturated solutions were prepared and the supernatant was diluted to conduct UV–Vis test, and the solubility was extrapolated based on the calculated standard curves. The conductivity measurements were carried out at room temperature using conductivity meter (INESA DDS-307A, China) with 0.01 M active materials or supporting electrolyte in MeCN.

Diffusion coefficient (D): The diffusion coefficients of active materials were calculated according to modified Randles-Sevcik equation[3]:

$$i_p = (2.69 \times 10^5)ACD^{1/2}v^{1/2}K(\Lambda, \alpha) \tag{1}$$

Where i_p is the peak current density, A the electrode surface area (0.07 cm^2), C the concentration of the active species (1.0 mM), D the diffusion coefficient, v the scan rate, and K(Λ,α) is the parameter associated with electrochemical irreversibility (K(Λ,α) = 0.8 when the transfer coefficient α delivered as 0.5).

Kinetic rate constant (k^0): The kinetic-controlled current i_k was first calculated according to Koutecký-Levich equation[3]:

$$\frac{1}{i} = \frac{1}{i_k} + \frac{1}{i_l} \tag{2}$$

where i_l is the diffusion-controlled limiting current and i the apparent current.

Then, according to the Tafel equation, the linearly fitted plots of log i_k versus η can be obtained to calculate the exchange current i^0:

$$\eta = -\frac{2.3RT}{\alpha nF}\log i^0 + \frac{2.3RT}{\alpha nF}\log i_k \tag{3}$$

where n is the number of electrons involved in an electrode reaction, F the Faradaic constant (F = 96485 C mol^{-1}).

Finally, the reaction rate constant k^0 can be calculated according to the following equation:

$$i^0 = nFAk^0C \tag{4}$$

4. Computation methods

The density functional theory (DFT) calculations were carried out using the Gaussian 09 package[4]. The geometry optimizations and single point energy calculations were calculated at the Grimme dispersion corrected hybrid (B3LYP-D3) level of density functional theory with the 6-311G(d) and 6-311G(d, p) basis set considering implicit solvation model based on solute electron density (SMD), respectively. The atom contribution for molecular orbital based on Hirshfeld method was calculated through Multiwfn 3.7(dev) code[5]. The ion-pair distance was obtained from the shortest distance between the nitrogen atom of tetraalkylammonium cation and the counter anion. The binding energy (ΔE_{BE}) was calculated by the difference between the electronic energy (E) of the compounds and the isolated cations/anions in gas phase:

$$\Delta E_{BE} = E(compound) - E(cation) - E(anion)$$

Supporting Figures
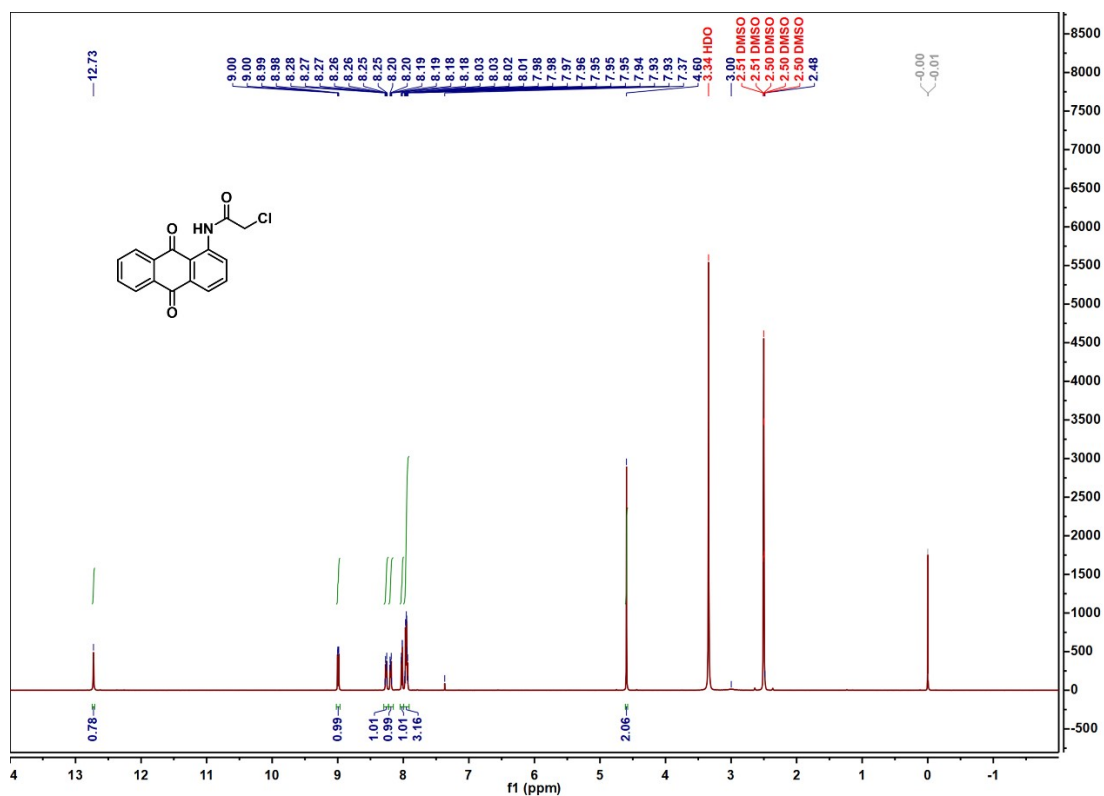
Fig. S1 ^{1}H NMR spectrum of 1-(Chloroacetylamido)-anthracene-9,10-dione in DMSO-d$_6$.
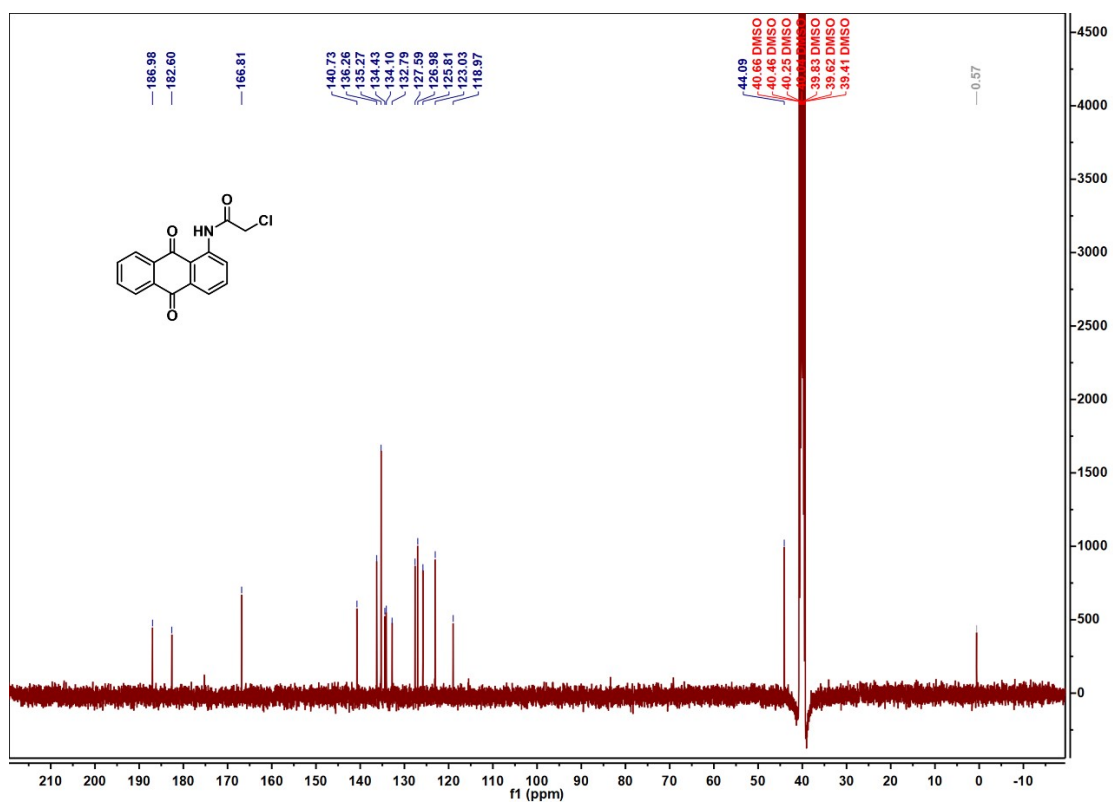
Fig. S2 ^{13}C NMR spectrum of 1-(Chloroacetylamido)-anthracene-9,10-dione in DMSO-d$_6$.
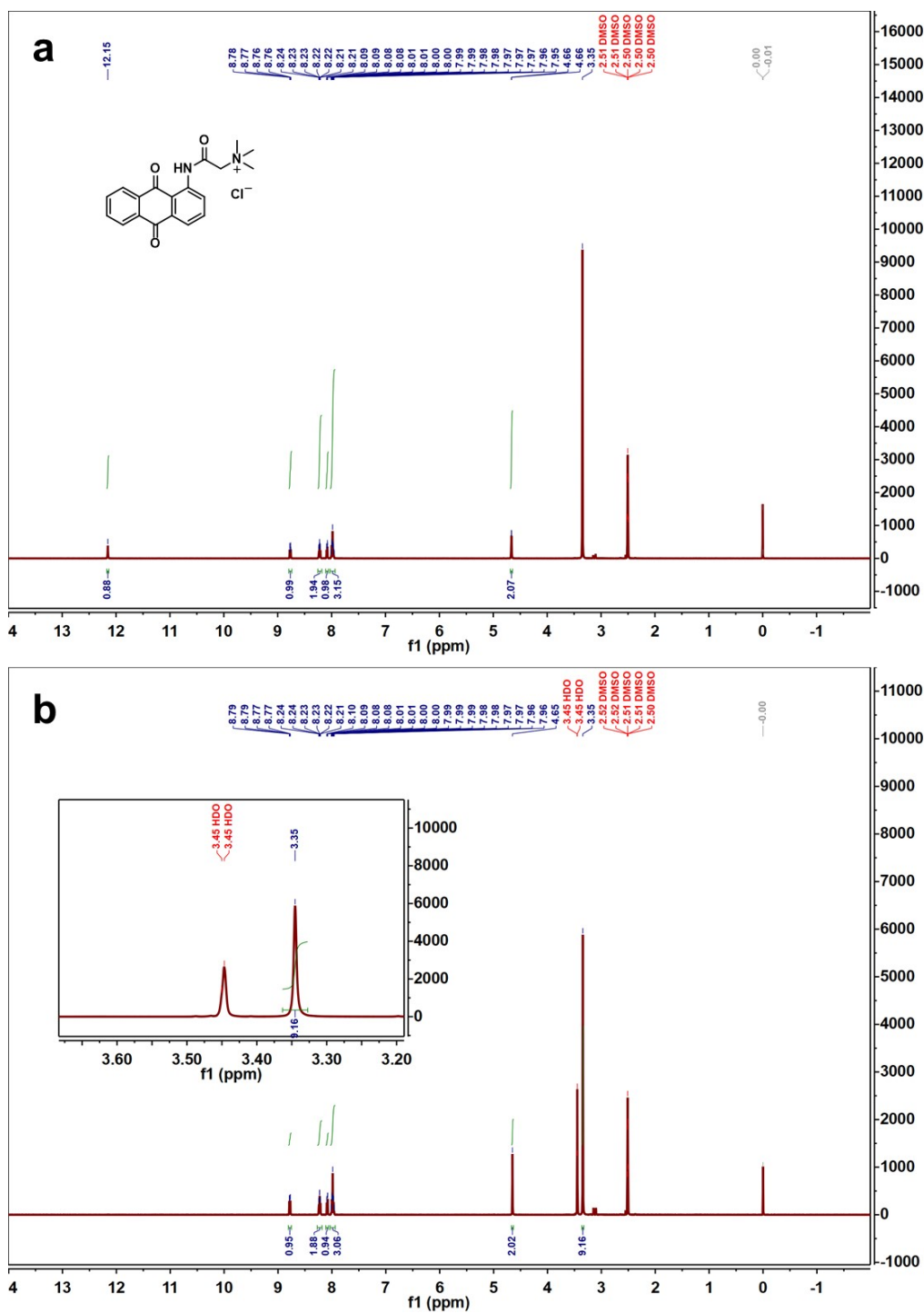
Fig. S3 ^{1}H NMR spectrum of acetamide, 2-(N,N,N-trimethylamino)-N-(9,10-dioxo-9,10-dihydroanthracen-1-yl)-, chloride in DMSO-d$_6$ before (a) and after (b) deuteroxide exchange.
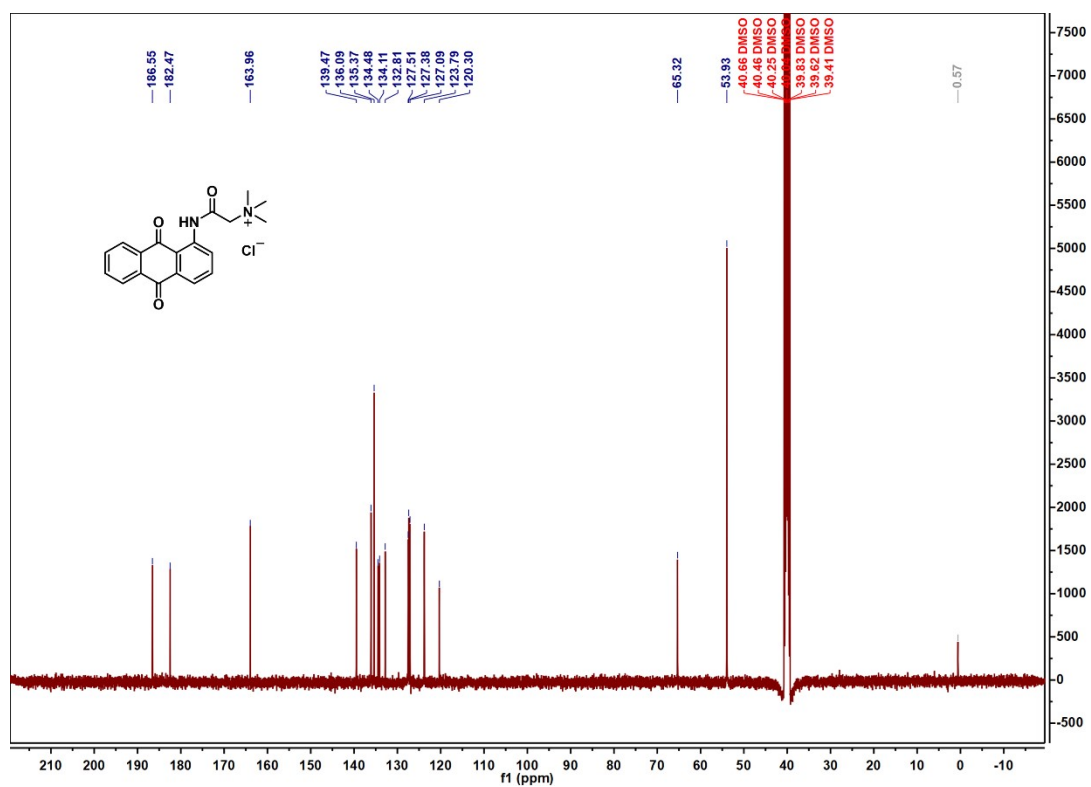
Fig. S4 ^{13}C NMR spectrum of acetamide, 2-(N,N,N-trimethylamino)-N-(9,10-dioxo-9,10-dihydroanthracen-1-yl)-, chloride in DMSO-d$_6$.
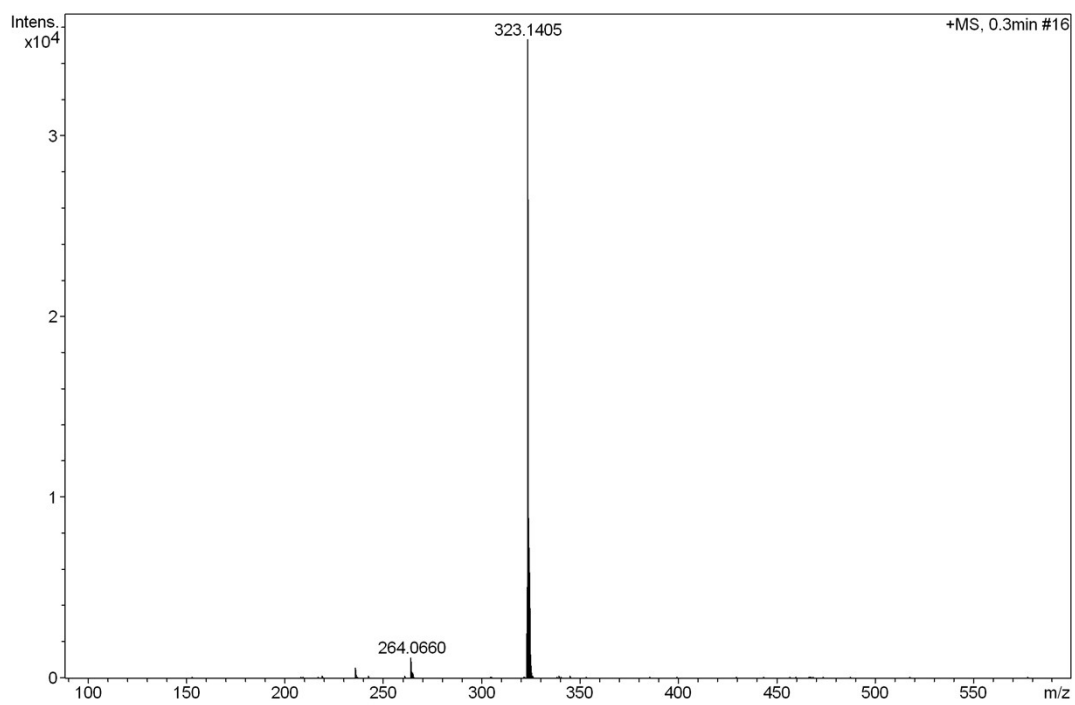
Fig. S5 HRMS (ESI) spectrum of AQNCl.
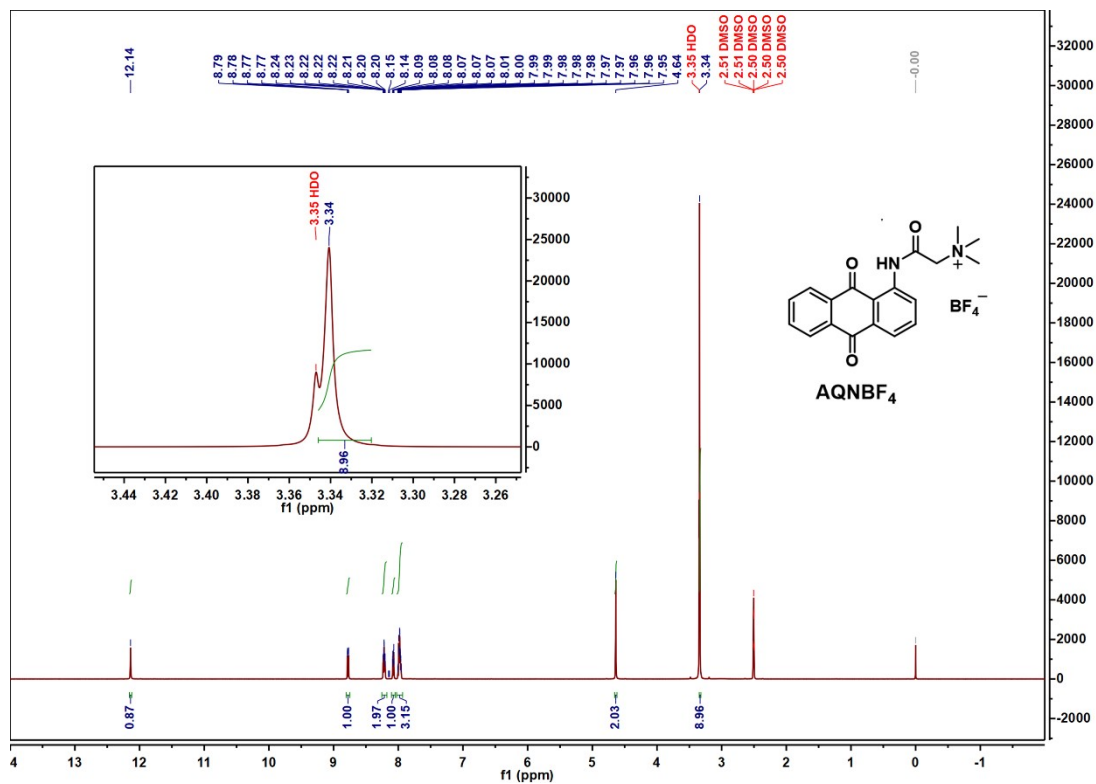
Fig. S6 ^{1}H NMR spectrum of AQNBF$_4$ in DMSO-d$_6$.
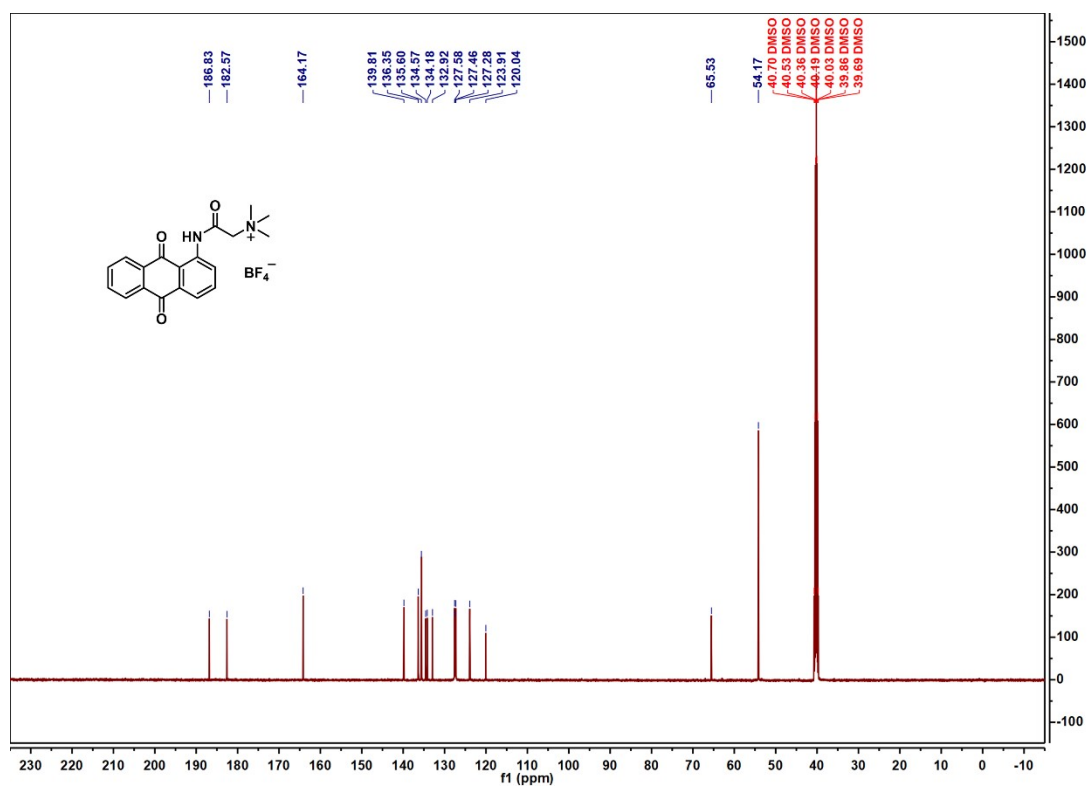
Fig. S7 ^{13}C NMR spectrum of AQNBF$_4$ in DMSO-d$_6$.
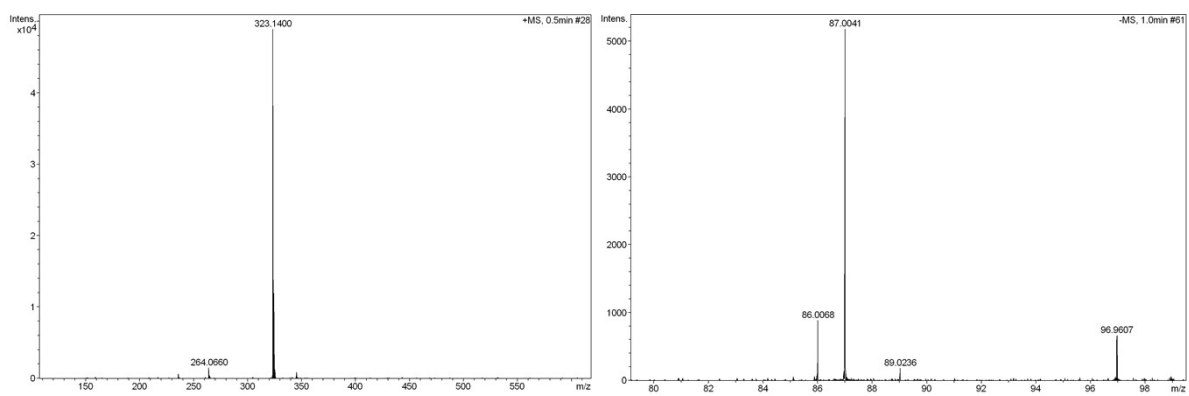
Fig. S8 HRMS (ESI) spectrum of AQNBF$_4$.
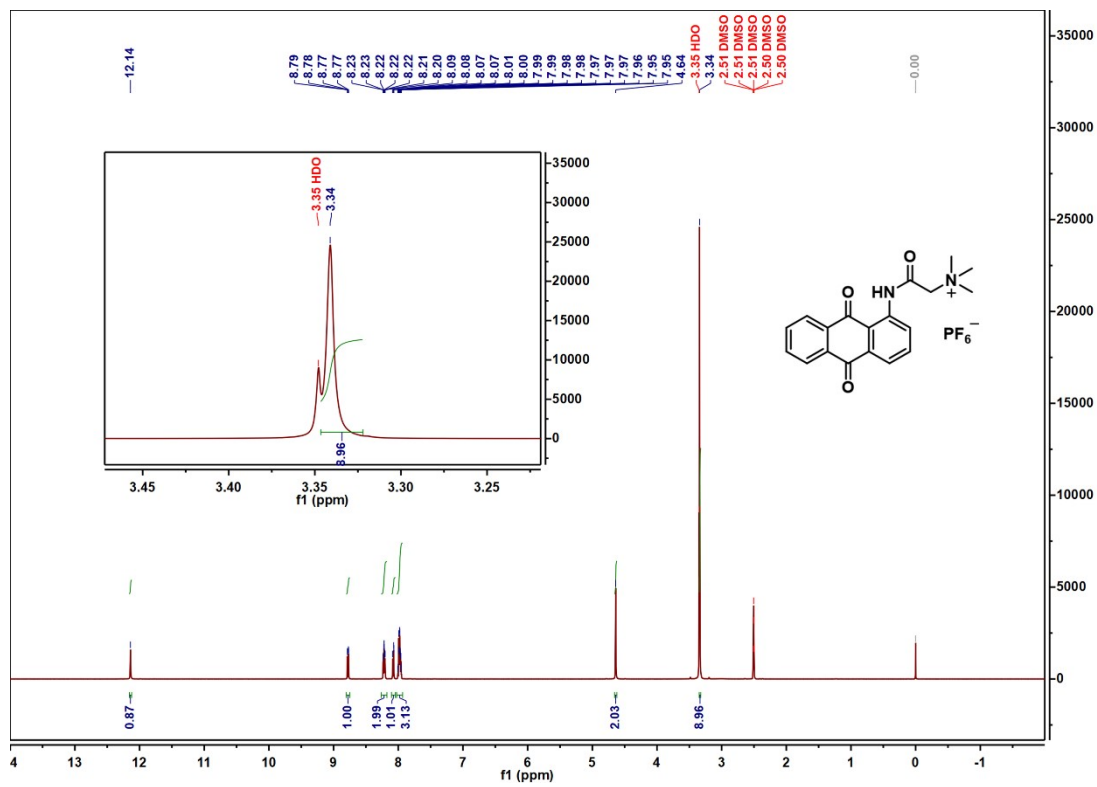
Fig. S9 ^{1}H NMR spectrum of AQNPF$_6$ in DMSO-d$_6$.
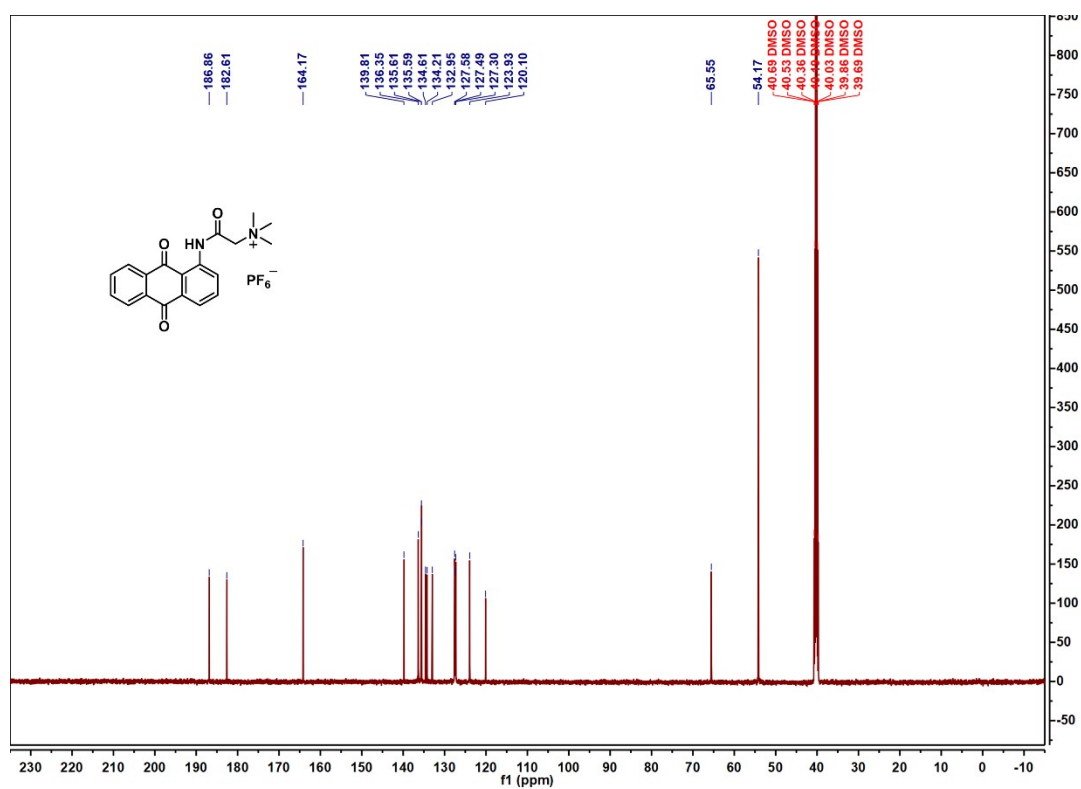
Fig. S10 ^{13}C NMR spectrum of AQNPF$_6$ in DMSO-d$_6$.
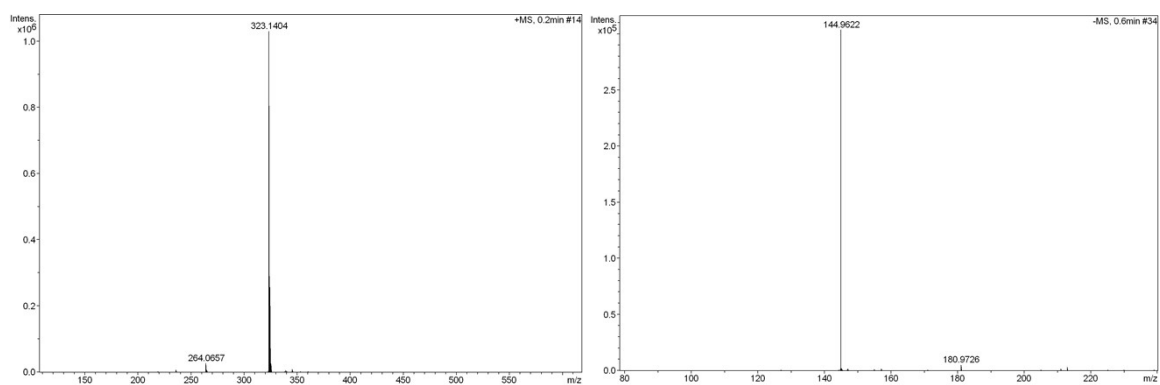
Fig. S11 HRMS (ESI) spectrum of AQNPF$_6$.
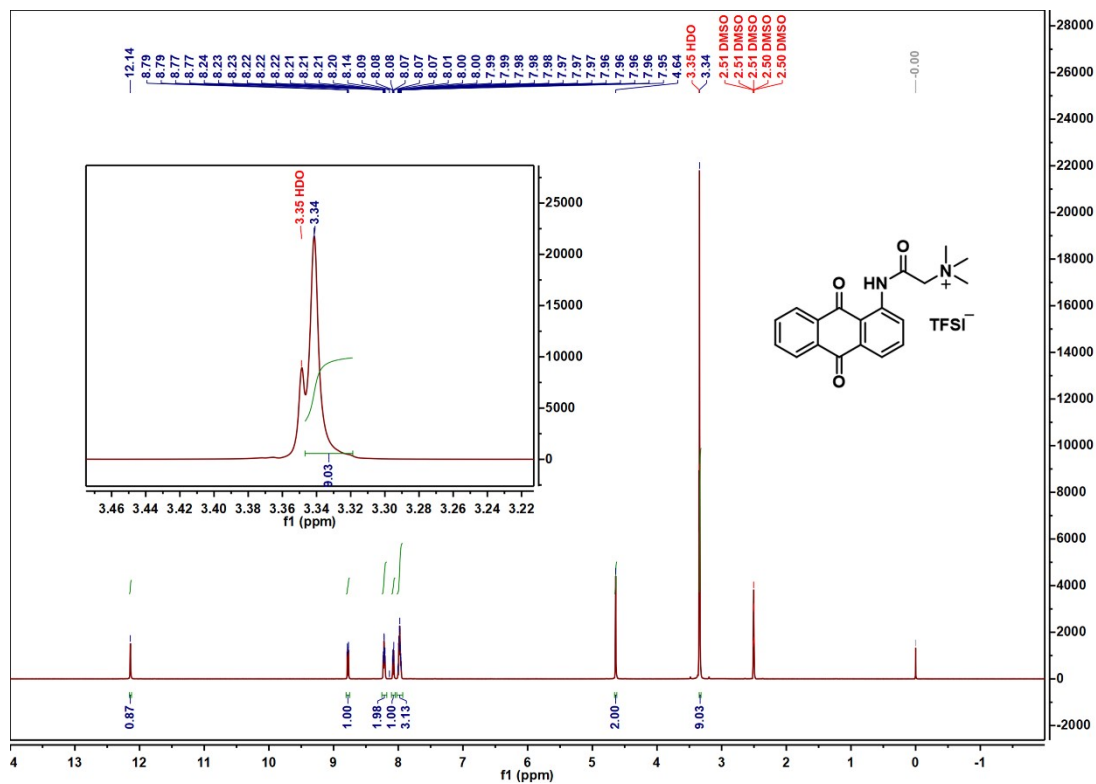
Fig. S12 ^{1}H NMR spectrum of AQNTFSI in DMSO-d$_6$.
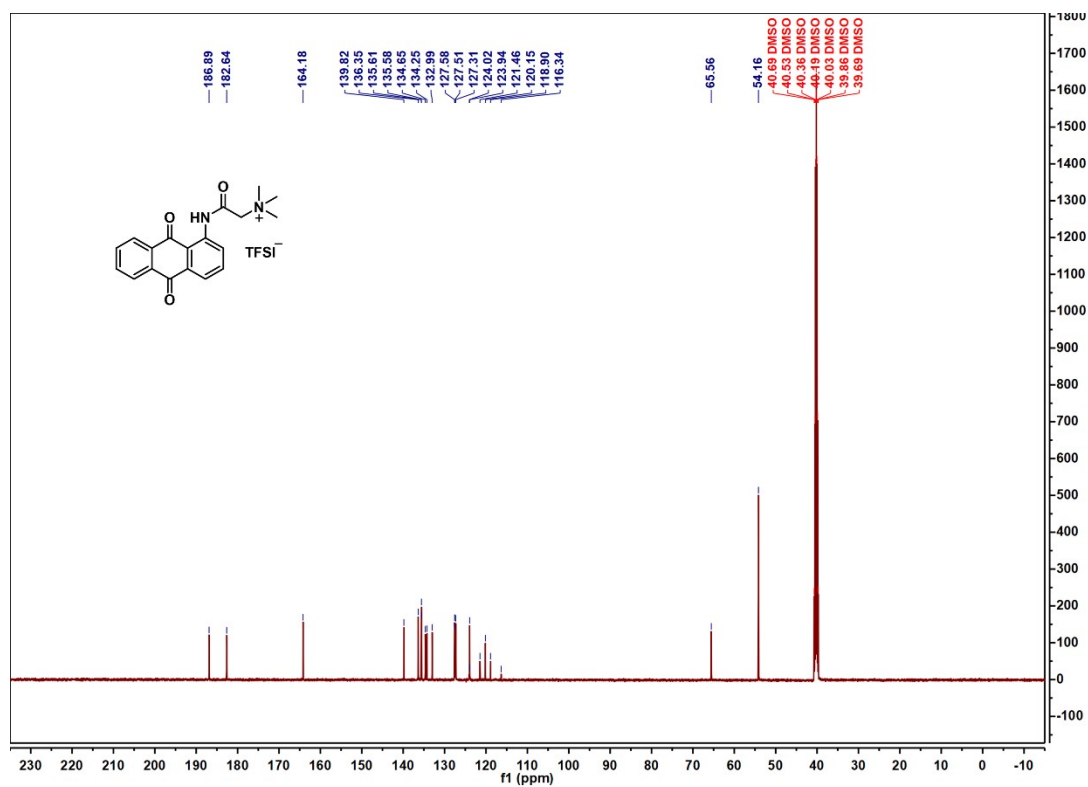
Fig. S13 ^{13}C NMR spectrum of AQNTFSI in DMSO-d$_6$.
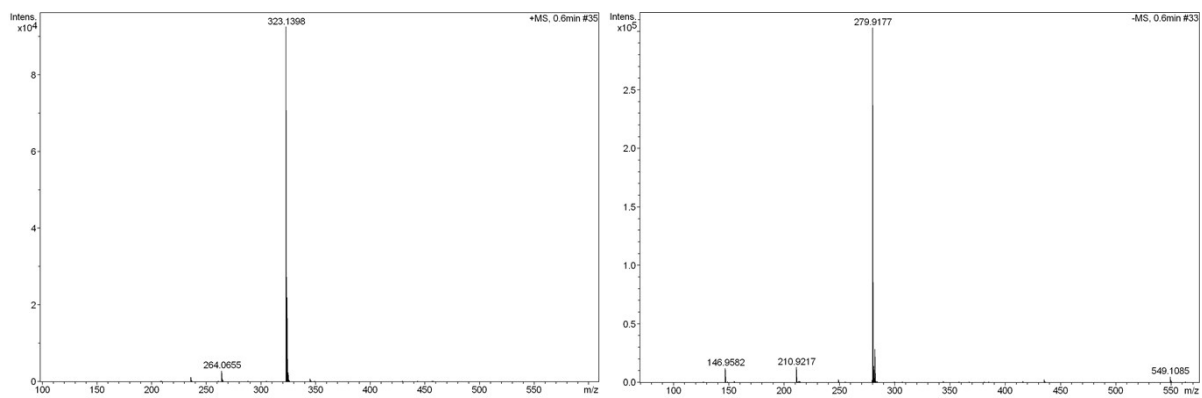
Fig. S14 HRMS (ESI) spectrum of AQNTFSI.
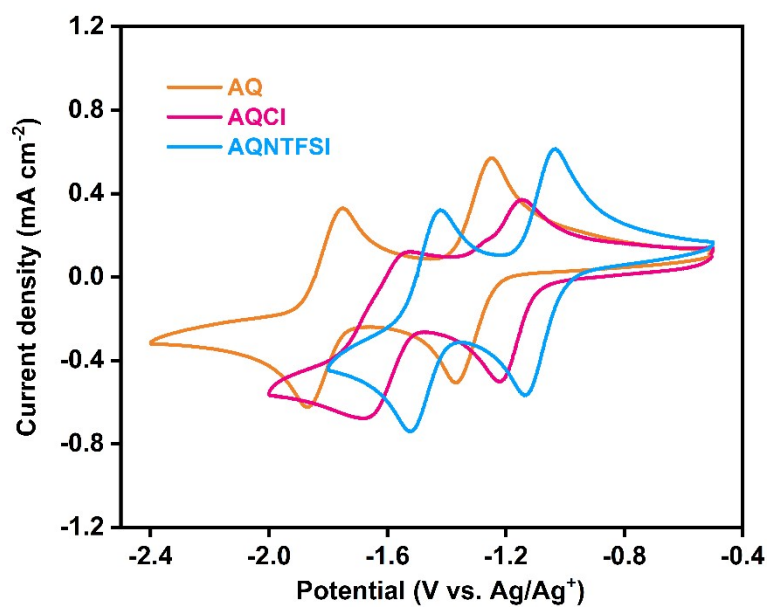
Fig. S15 CV curves of 1 mM AQ, AQCl, and AQNTFSI in 0.1 M TEATFSI/MeCN, respectively.
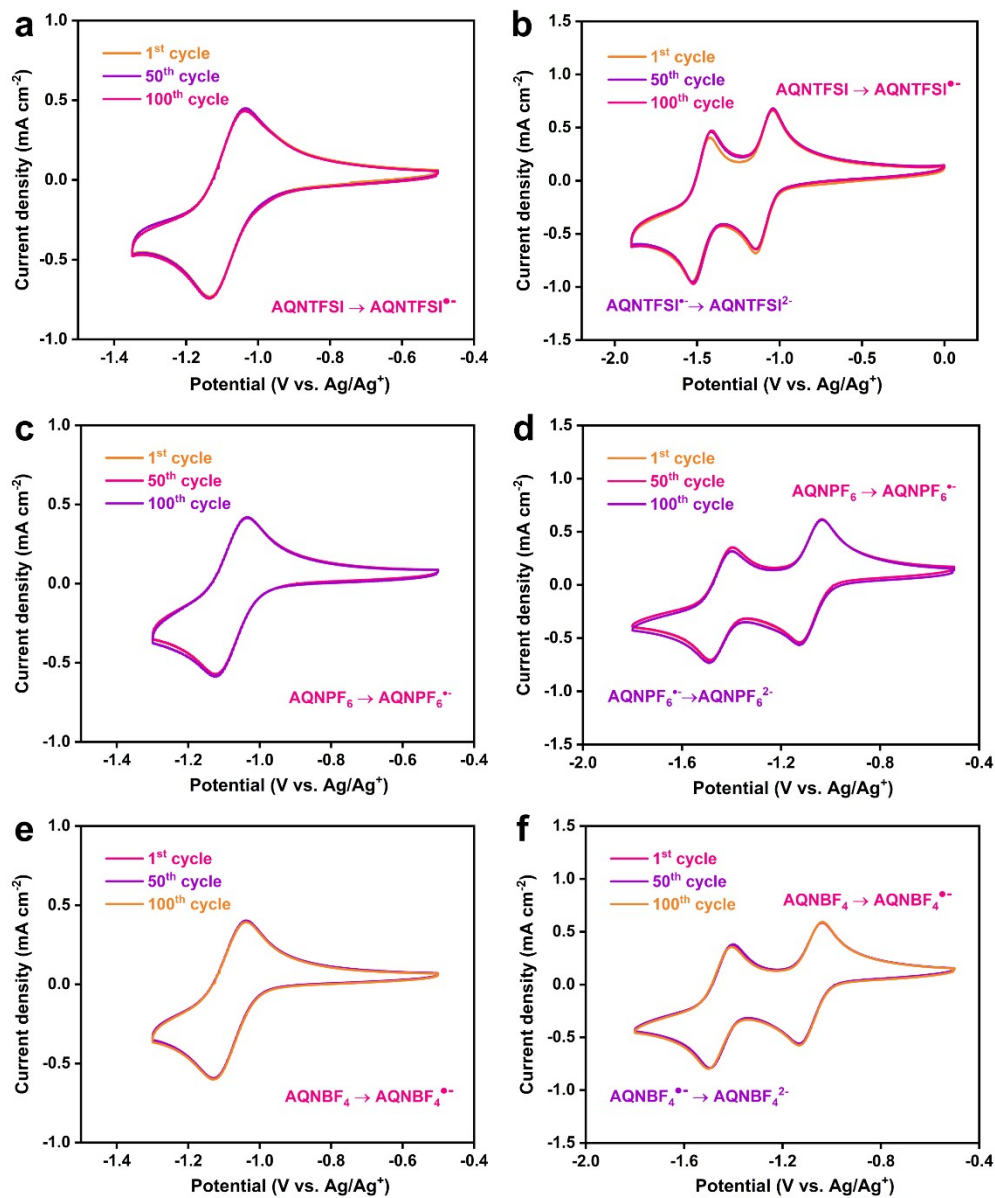
Fig. S16 CV curves of 1 mM AQNTFSI in 0.1 M TEATFSI/MeCN (a, b), 1 mM AQNPF$_6$ in 0.1 M TEAPF$_6$/MeCN (c, d) and 1 mM AQNBF$_4$ in 0.1 M TEABF$_4$/MeCN (e, f) over 100 cycles at the scan rate of 300 mV s^{-1} when 1e$^-$ (a, c, e) and 2e$^-$ (b, d, f) redox events are involved, respectively.
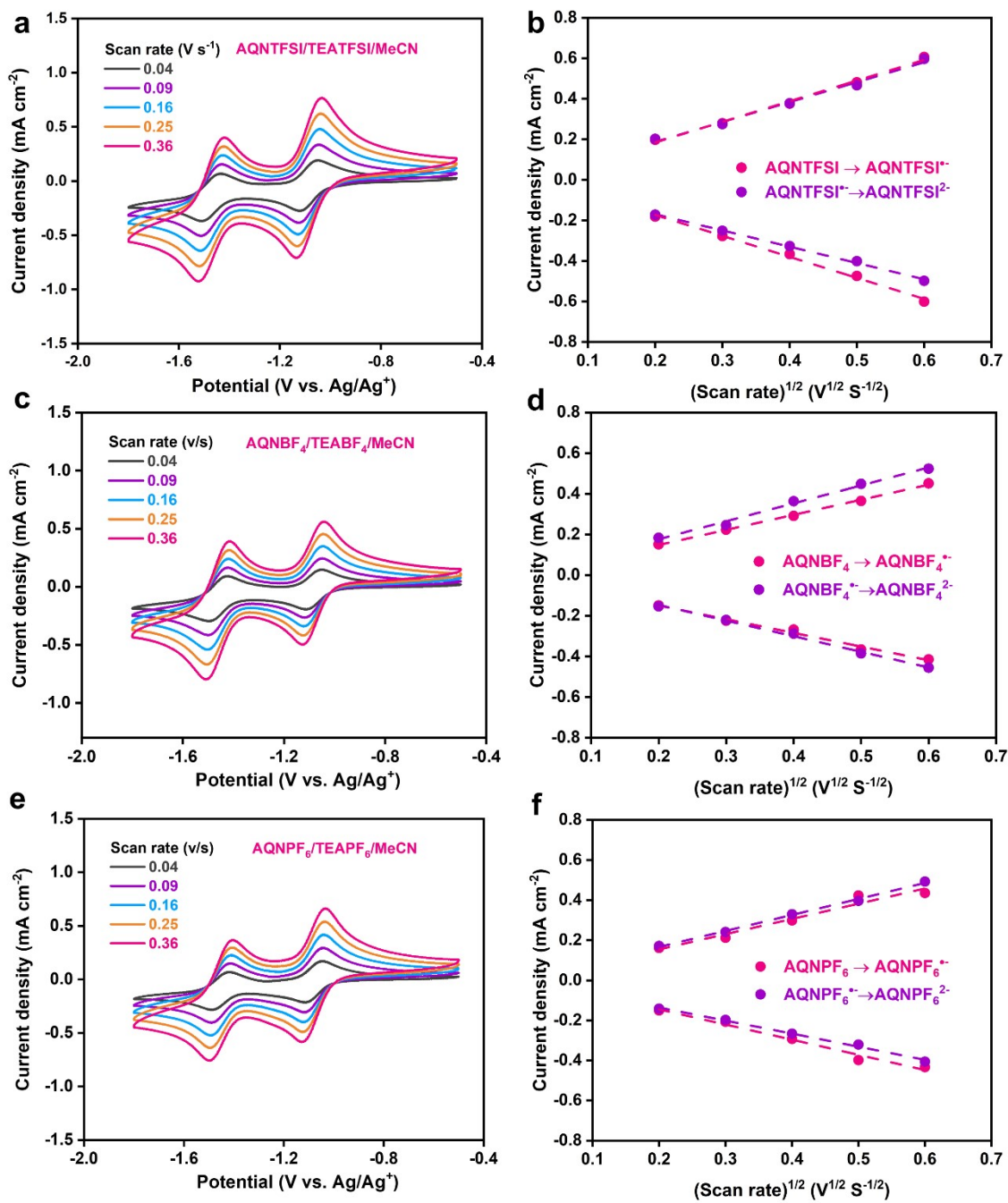
Fig. S17 CV curves of 1mM AQNTFSI /0.1 M TEATFSI/MeCN (a), 1 mM AQNBF$_4$/0.1 M TEABF$_4$/MeCN (c) and 1mM AQNPF$_6$ /0.1 M TEAPF$_6$/MeCN (e) at different scan rates (0.04, 0.09, 0.16, 0.25, 0.36 V s^{-1}). Linear relationship between peak current densities and the square root of scan rate for 1e$^-$ and 2e$^-$ redox reactions for AQNTFSI (b), AQNPF$_6$ (d) and AQNBF$_4$ (f).
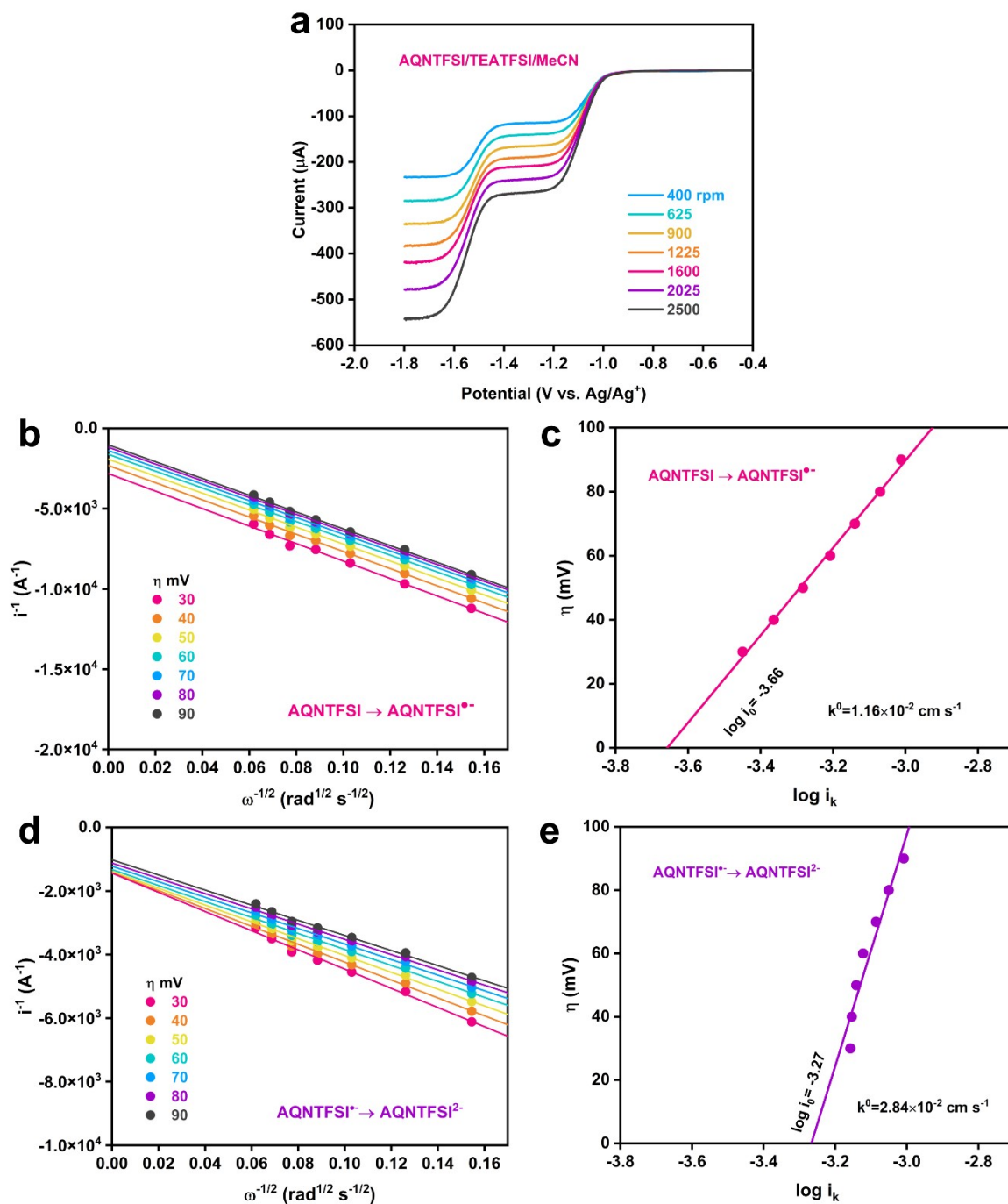
Fig. 18 (a) LSV curves of AQNTFSI at the scan rate of 10 mV s^{-1} with the working electrode being rotated from 400 to 2500 rpm. (b, d) Linearly fitted Koutecky-Levich plots of limiting current i_l vs. $\omega^{-1/2}$ for 1e$^-$ and 2e$^-$ redox reactions, respectively. (c, e) Linearly fitted plots of $\log i_k$ vs. overpotential (η) for 1e$^-$ and 2e$^-$ redox reactions, respectively.
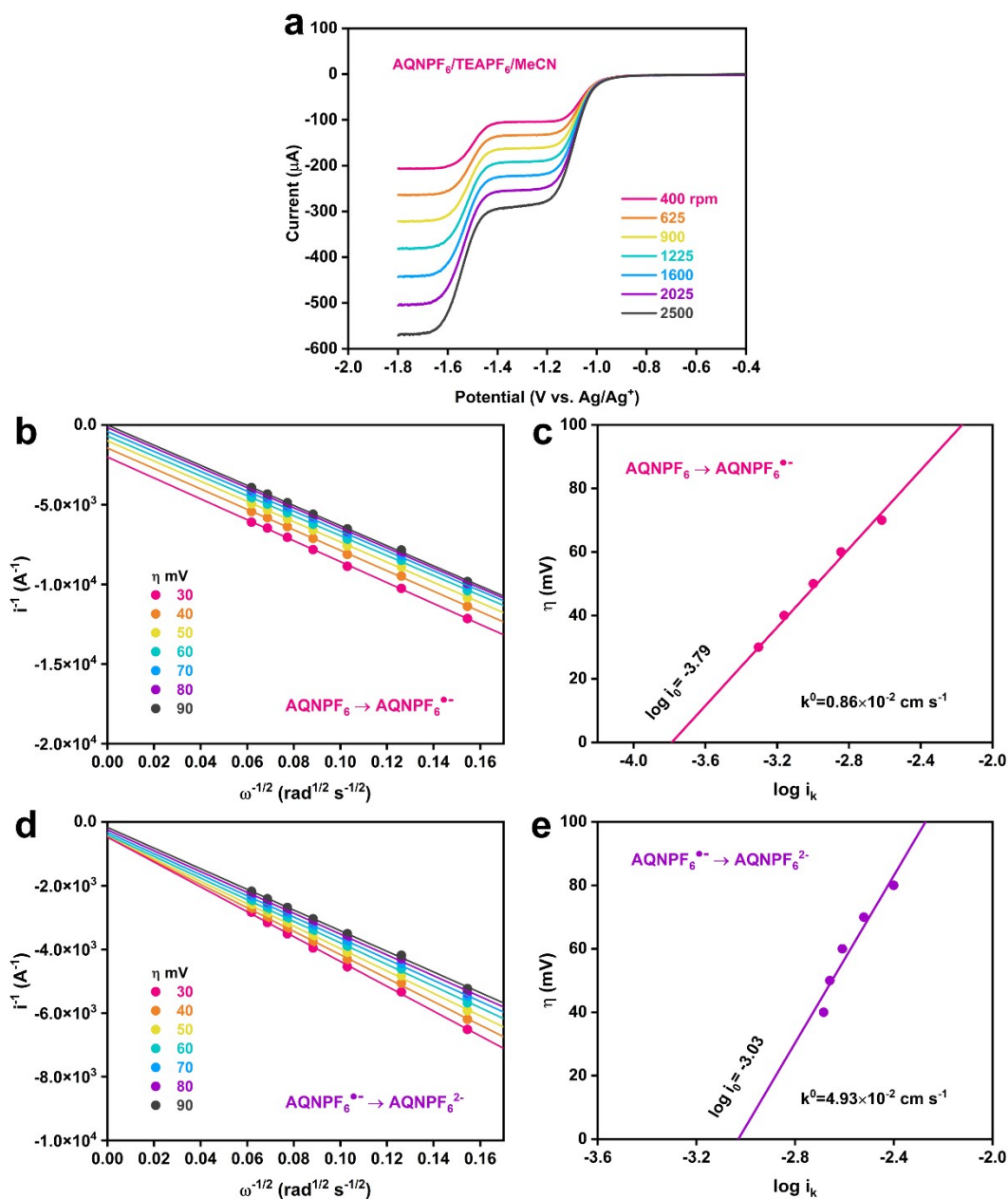
Fig. S19 (a) LSV curves of AQNPF$_6$ at the scan rate of 10 mV s^{-1} with the working electrode being rotated from 400 to 2500 rpm. (b, d) Linearly fitted Koutecky-Levich plots of limiting current i_l vs. $\omega^{-1/2}$ for 1e$^-$ and 2e$^-$ redox reactions, respectively. (c, e) Linearly fitted plots of $\log i_k$ vs. overpotential (η) for 1e$^-$ and 2e$^-$ redox reactions, respectively.
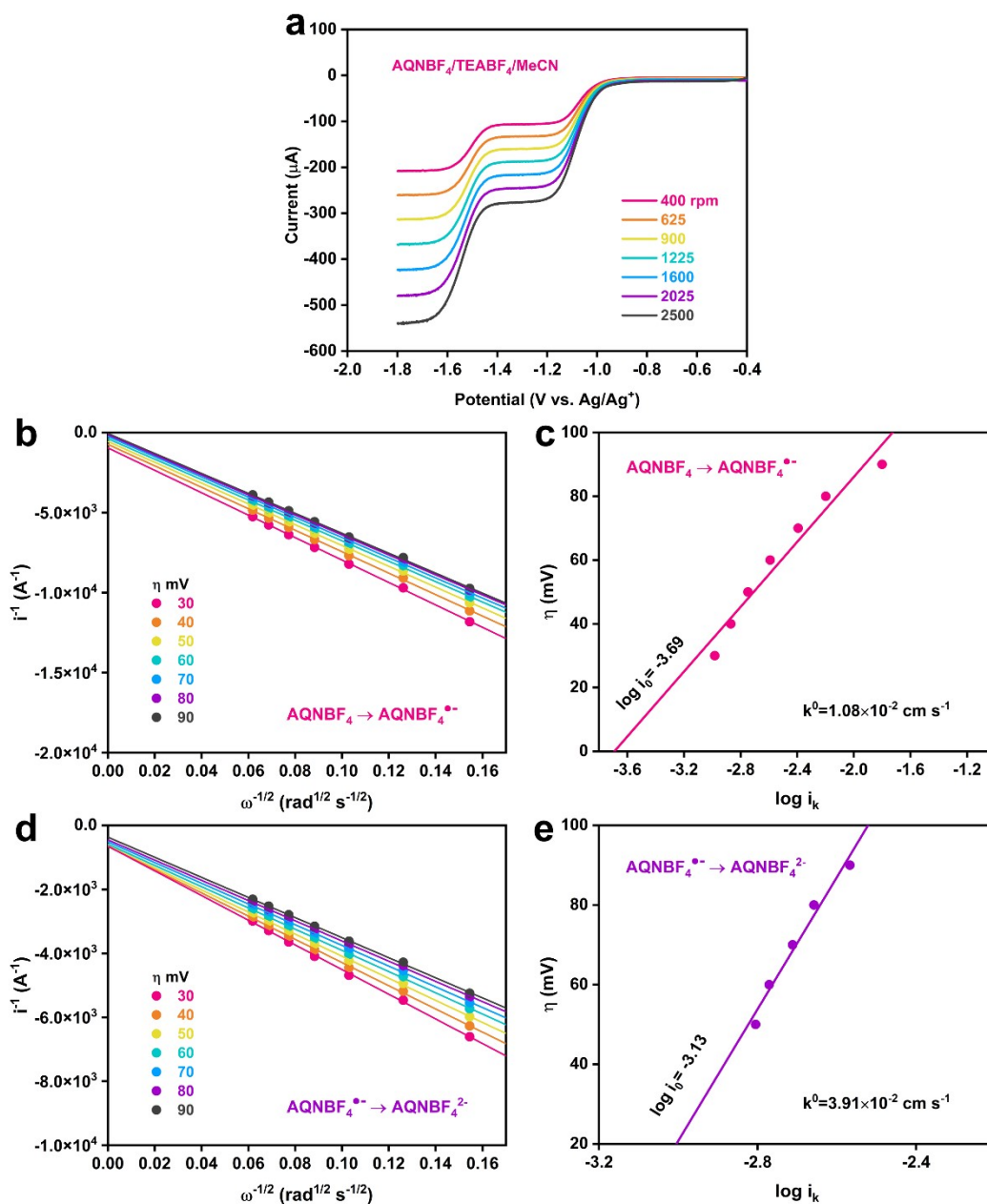
Fig. S20 (a) LSV curves of AQNBF$_4$ at the scan rate of 10 mV s^{-1} with the working electrode being rotated from 400 to 2500 rpm. (b, d) Linearly fitted KouteckyLevich plots of limiting current i_l vs. ω$^{-1/2}$ for 1e$^-$ and 2e$^-$ redox reactions, respectively. (c, e) Linearly fitted plots of $\log i_k$ vs. overpotential (η) for 1e$^-$ and 2e$^-$ redox reactions, respectively.
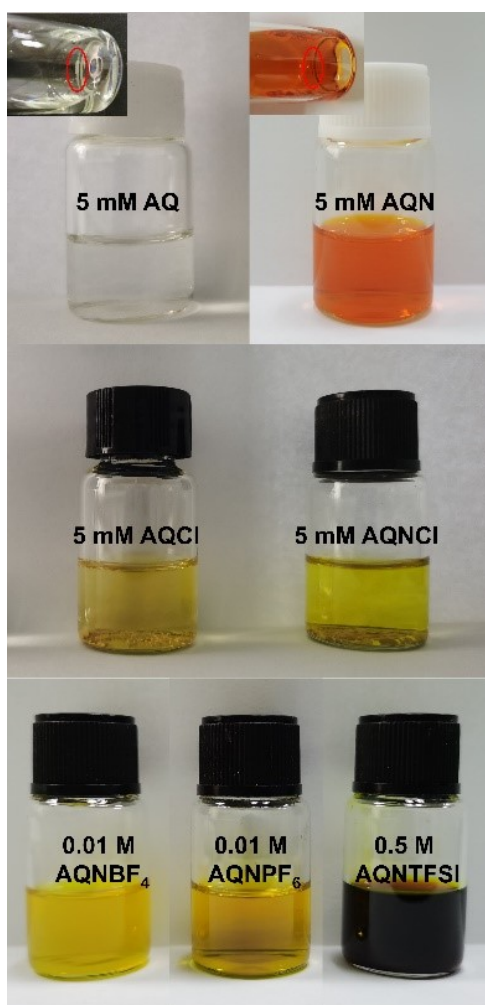
Fig. S21 Photos of AQ, AQN, AQCl, AQNCl, AQNBF$_4$, AQNPF$_6$ and AQNTFSI dissolved in MeCN.

The areas marked by the red circles are undissolved species.
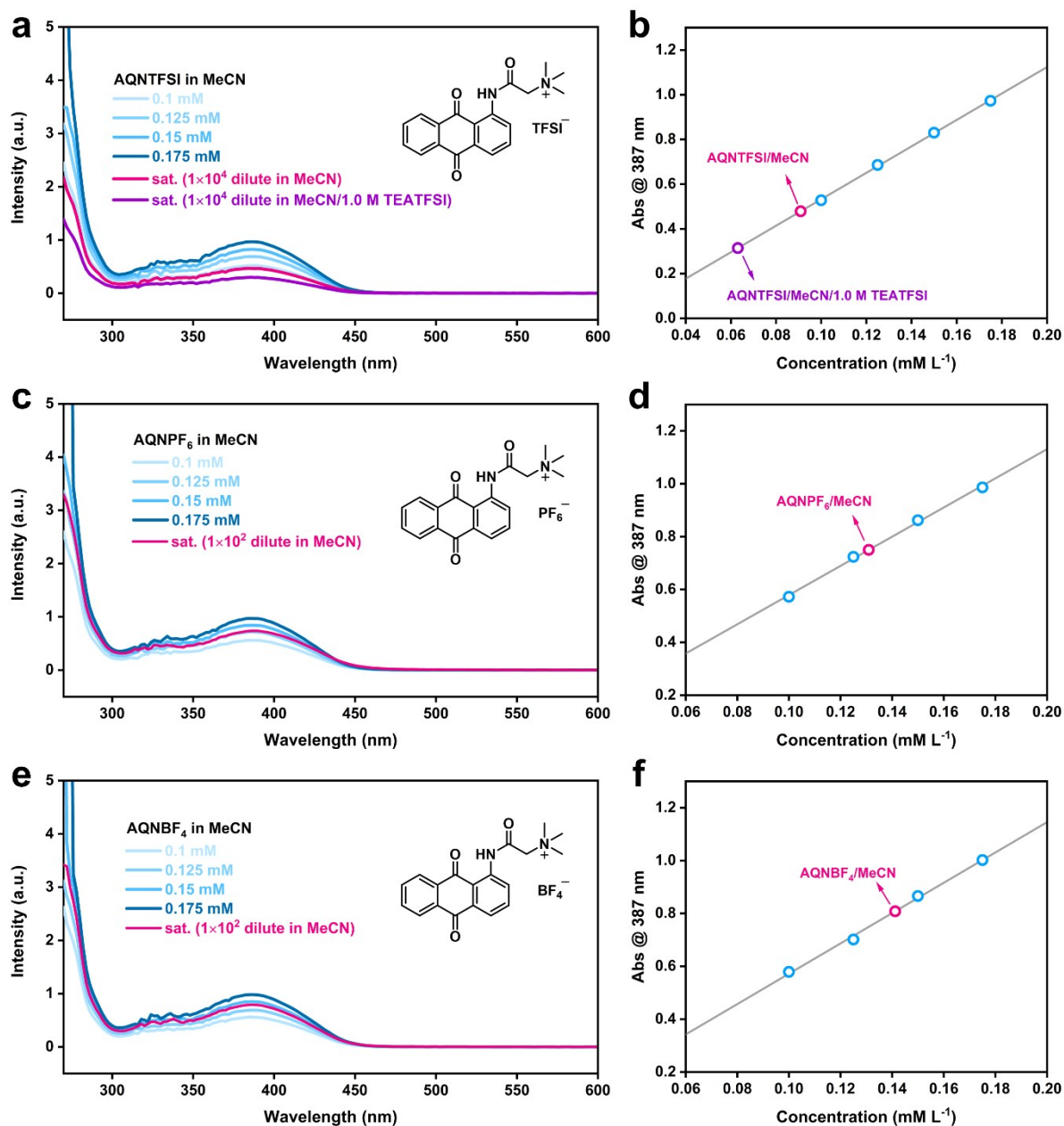
Fig. S22 UV-Vis spectra (a, c, e) and standard curves (b, d, f) of AQNTFSI, AQNPF$_6$ and AQNBF$_4$ in MeCN, respectively.
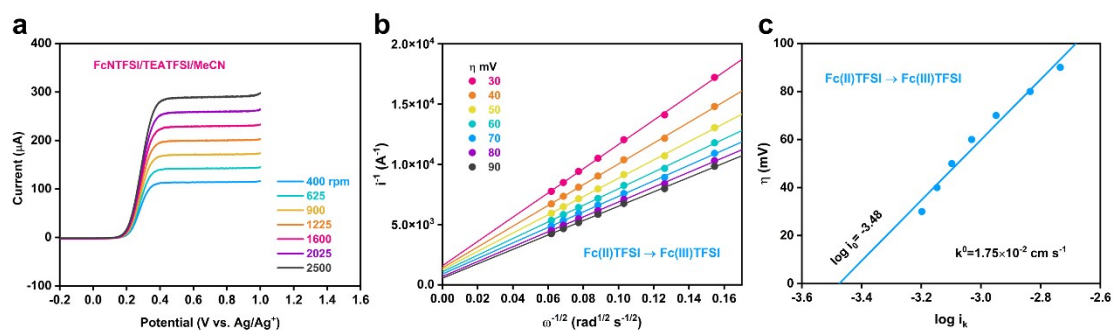
Fig. S23 (a) LSV curves of FcNTFSI at the scan rate of 10 mV s^{-1} with the working electrode being rotated from 400 to 2500 rpm. (b) Linearly fitted Koutecky-Levich plots of limiting current i_l vs. $\omega^{-1/2}$. (c) Linearly fitted plots of $\log i_k$ vs. overpotential (η).
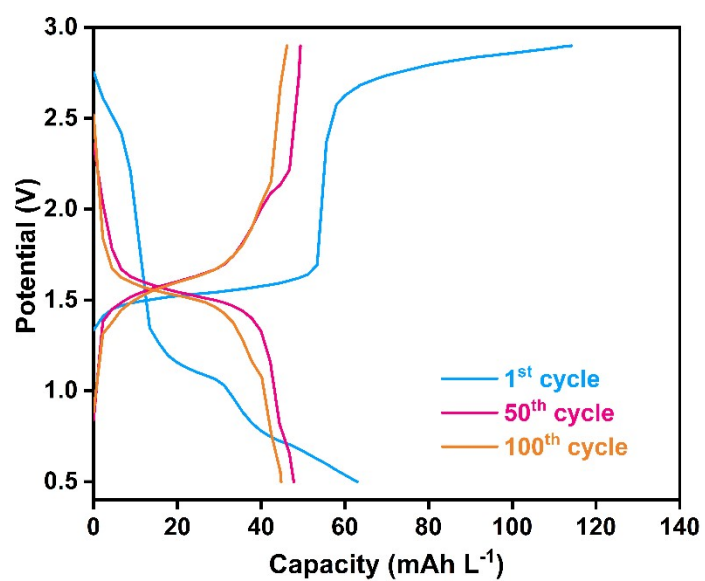
Fig. S24 Galvanostatic charge/discharge profiles of the battery using Daramic AA-800 membrane with mixed-reactant electrolyte of 1.0 mM AQ/2.0 mM FcNTFSI in 0.1 M TEATFSI/MeCN at the current density of 2 mA cm^{-2}.
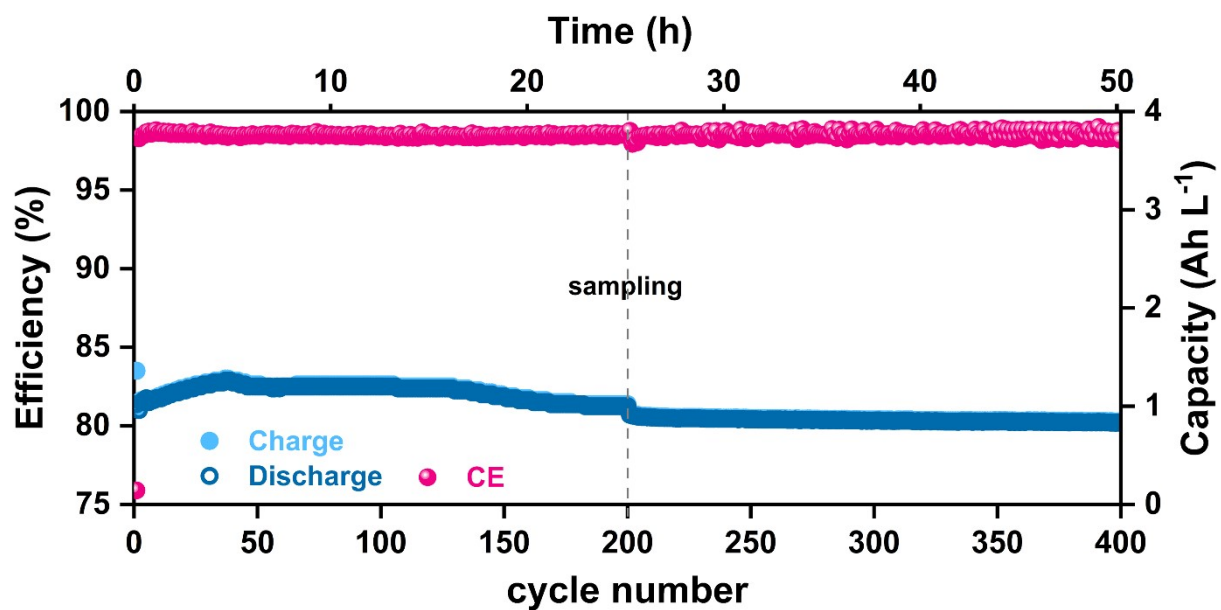
Fig. S25 Cycling profile of the battery over 400 cycles using Daramic AA-800 membrane with mixed-reactant electrolyte of 0.025 M AQNTFSI/0.05 M FcNTFSI in 0.5 M TEATFSI/MeCN at the current density of 20 mA cm^{-2}. Sampling was carried out at 200th cycle to perform UV-Vis and NMR test.
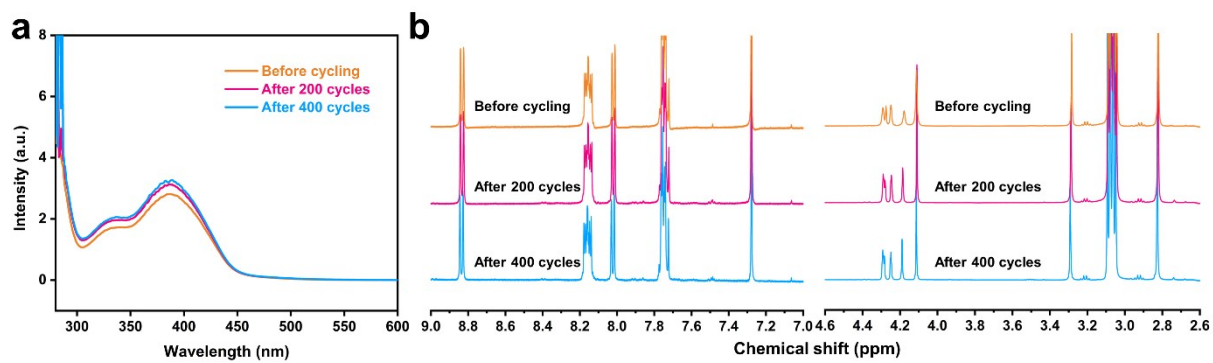
Fig. S26 UV-Vis (a) and 1H NMR (b) spectrum of the fresh, 200- and 400-cycled anolyte.
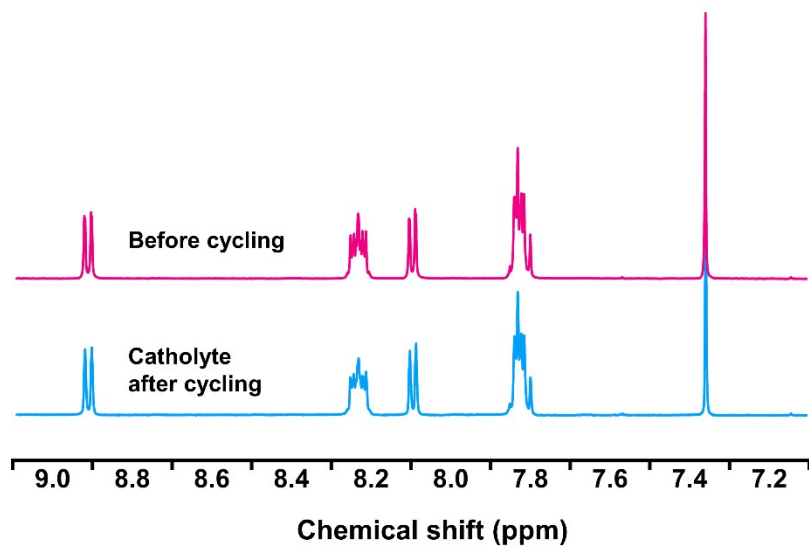
Fig. S27 1H NMR spectrum of AQNTFSI in the catholyte before and after cycling tests.
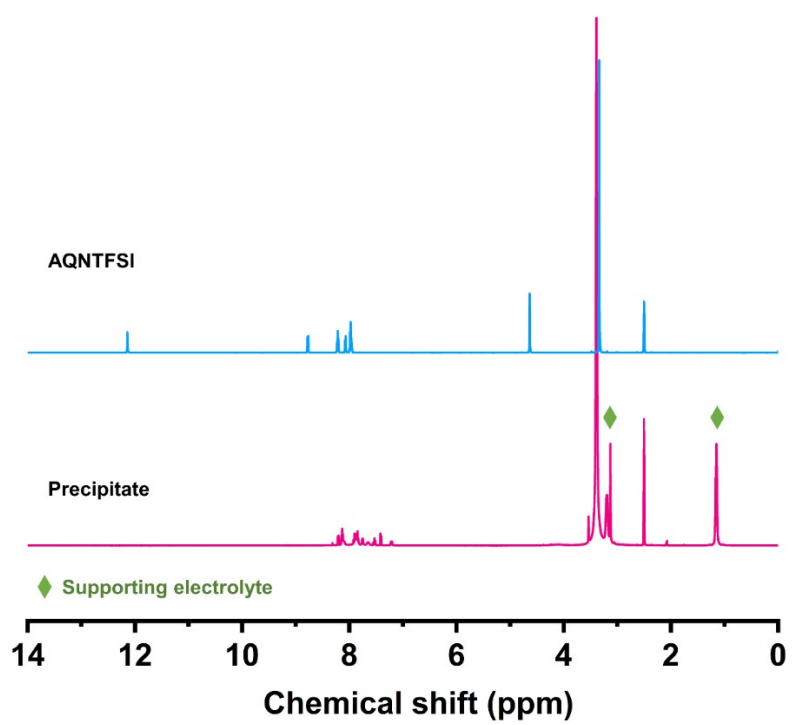
Fig. S28 ^{1}H NMR spectrum of the precipitate in DMSO-d$_6$.
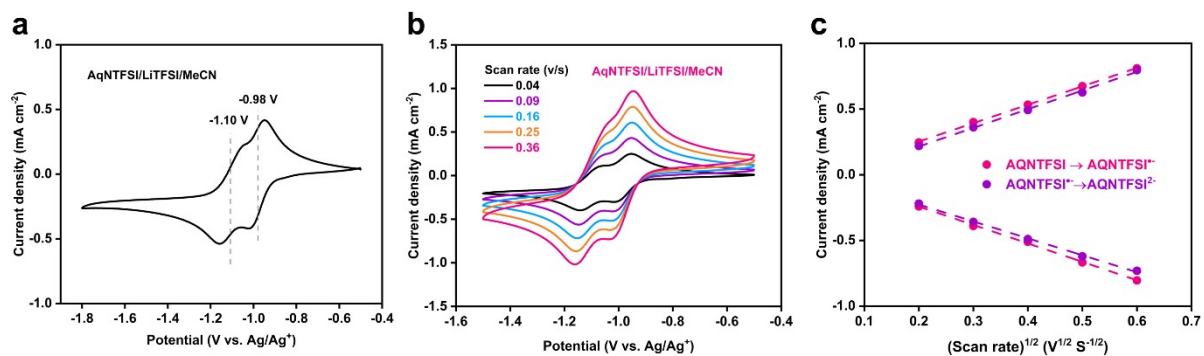
Fig. S29 (a) CV curves of 1 mM AQNTFSI /0.1 M LiTFSI/MeCN. (b) CV curves at different scan rates (0.04, 0.09, 0.16, 0.25, 0.36 V s^{-1}). (c) Linear relationship between peak current densities and the square root of scan rate for 1e$^-$ and 2e$^-$ redox reactions.
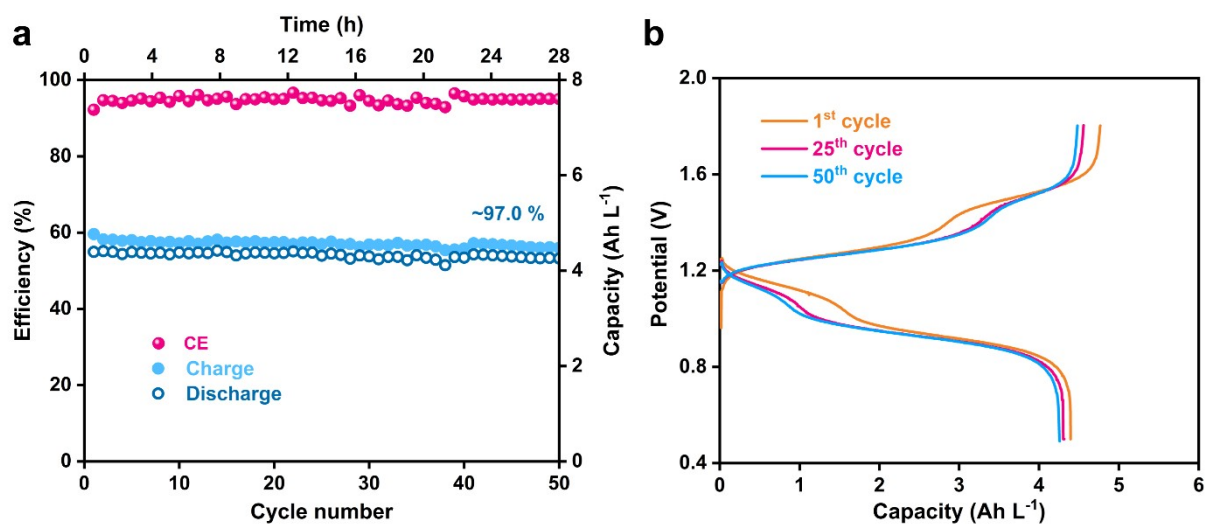
Fig. S30 (a) Cycling performance of the battery over 50 cycles using Daramic AA-800 membrane with mixed-reactant electrolyte 0.1 M AQNTFSI/0.2 M FcNTFSI in 0.5 M LiTFSI/MeCN at the current density of 20 mA cm^{-2}. (b) Galvanostatic charge/discharge profiles at selected cycles.

Table S1. Battery performance comparison of 2e⁻ electron transfer NARFB.

Electrolyte	Electron transfer number	Voltage (V)	Cycle No.	CE/EE (%)	Capacity retention (%)	J (mA cm^{-2})	Ref.
0.05 M DMPZ/0.1 M FL/0.5 M LiTFSI	2	2.0	30	90/70	-	20	[6]
0.1 M MVTFSI/0.2 M FcNTFSI/ 1.0 M LiTFSI	2	1.5	100	-/71.4	88.3	30	[7]
0.05 M PT3/0.05 M AQ4/1.0 M TEABF$_4$	2	2.8	10	91/81	-	10	[8]
0.05 M BMEPZ/0.1 M FL/0.5 M LiTFSI	2	2.0	200	96/70	~87.5	20	[9]
0.01 M PEG12-V /0.05 M PEG12-PTZ /0.5 M TBAPF$_6$	2	1.54	300	99.7/72.7	69.0	2	[10]
0.025 M AQNTFSI/0.05 M FcNTFSI/0.5 M TEATFSI	2	1.72	200	96.8/82.4	86.0	10	This work
0.1 M AQNTFSI/0.2 M FcNTFSI/0.5 M TEATFSI	2	1.72	100	98.1/52.9	78.5	20	This work

DFT calculation results

Coordinates of optimized structures of AQNTFSI

C	7.486803	-2.2601	-1.27786
C	7.941633	-1.176	-2.03416
C	7.272701	0.040735	-1.98137
C	6.150941	0.185863	-1.16115
C	5.691276	-0.90282	-0.40335
C	6.361591	-2.12825	-0.47351
C	5.449309	1.493136	-1.11093
C	4.336931	1.643615	-0.11402
C	3.884713	0.556273	0.665071
C	4.464895	-0.80375	0.434045
C	3.796607	2.918596	0.050343
C	2.823406	3.144829	1.01399
C	2.387774	2.092146	1.811071
C	2.895816	0.801541	1.645594
O	3.950214	-1.81523	0.888302
O	5.781956	2.42628	-1.818
N	2.414508	-0.18993	2.54933
C	1.662044	-1.30752	2.306723
C	1.174849	-1.51681	0.872978
N	-0.32619	-1.36124	0.744816
O	1.332419	-2.06052	3.201013
C	-1.07206	-2.52013	1.363689
C	-0.7749	-0.07957	1.402437
C	-0.64882	-1.3138	-0.7303
H	1.613121	-0.80934	0.17579
H	1.443235	-2.52443	0.564938
H	8.010197	-3.20913	-1.32135
H	8.816626	-1.2847	-2.66583
H	7.600617	0.89209	-2.56579
H	5.984923	-2.96183	0.106696
H	4.163116	3.717709	-0.58208
H	2.399998	4.134178	1.144986
H	1.630478	2.254309	2.5703
H	2.625396	-0.05897	3.530445
H	-0.76477	-2.62045	2.399457
H	-2.13977	-2.32039	1.285941
H	-0.8126	-3.42354	0.813297
H	-0.59309	-0.15841	2.471767
H	-0.2185	0.749622	0.970588
H	-1.8335	0.044609	1.196073
H	-1.72703	-1.31057	-0.84337
H	-0.2597	-0.39067	-1.15245
H	-0.20159	-2.18682	-1.2037

N	-3.43576	-0.00207	-0.16755
S	-3.33481	1.372349	-1.01235
S	-4.75785	-0.86141	0.190194
O	-1.92216	1.509597	-1.37981
O	-4.36379	-1.75483	1.28203
O	-6.01794	-0.13971	0.242828
O	-4.37816	1.61761	-1.9943
C	-3.56391	2.677192	0.329296
C	-4.86915	-2.01145	-1.29857
F	-3.44686	3.895962	-0.20112
F	-4.75083	2.562151	0.914591
F	-2.6067	2.530906	1.269246
F	-3.72028	-2.71469	-1.40278
F	-5.04441	-1.32606	-2.42409
F	-5.87508	-2.87088	-1.14073

Coordinates of optimized structures of AQNPF$_6$

C	6.370098	-1.44296	-1.89512
C	6.845574	-0.14758	-2.1187
C	6.166849	0.944789	-1.5927
C	5.013951	0.748393	-0.82822
C	4.533082	-0.55166	-0.60582
C	5.214385	-1.64479	-1.15072
C	4.30332	1.924335	-0.26705
C	3.152708	1.659944	0.660549
C	2.67209	0.35299	0.895845
C	3.27466	-0.79616	0.150186
C	2.60382	2.757509	1.322667
C	1.590578	2.575215	2.254006
C	1.121629	1.293122	2.51706
C	1.639479	0.181801	1.847093
O	2.753823	-1.90198	0.130674
O	4.656214	3.063196	-0.51168
N	1.12179	-1.08763	2.235934
C	0.395141	-2.00125	1.520832
C	-0.00939	-1.61007	0.099579
N	-1.50695	-1.44441	-0.05835
O	0.02842	-3.04884	2.014473
C	-2.2361	-2.76517	0.017268
C	-2.03765	-0.52512	1.015624
C	-1.74672	-0.84658	-1.42673
H	0.433979	-0.67058	-0.21671
H	0.321096	-2.39631	-0.57457
H	6.901438	-2.29404	-2.30718
H	7.74445	0.006229	-2.70587

H	6.51102	1.958471	-1.75958
H	4.82229	-2.64028	-0.98153
H	2.995774	3.741887	1.098389
H	1.161848	3.425384	2.7724
H	0.331288	1.134803	3.242744
H	1.275276	-1.36998	3.195698
H	-2.02287	-3.2328	0.972453
H	-3.29584	-2.55714	-0.10461
H	-1.87524	-3.40096	-0.7901
H	-1.86749	-0.99684	1.980873
H	-1.51055	0.424687	0.951718
H	-3.09463	-0.36266	0.857579
H	-2.81297	-0.81674	-1.61098
H	-1.35766	0.168328	-1.44181
H	-1.2335	-1.46913	-2.15864
P	-5.3033	0.654533	-0.63326
F	-5.0821	0.642307	0.998628
F	-3.7342	1.198046	-0.78652
F	-4.68463	-0.91968	-0.65864
F	-5.4146	0.596385	-2.25252
F	-6.79127	0.053192	-0.46041
F	-5.83706	2.17579	-0.58788

Coordinates of optimized structures of AQNBF$_4$

C	-3.36094	3.808774	1.070153
C	-4.4457	3.761015	0.189943
C	-4.72774	2.592306	-0.50691
C	-3.9334	1.458417	-0.31868
C	-2.84124	1.505911	0.562748
C	-2.55632	2.690194	1.249968
C	-4.24714	0.216802	-1.06771
C	-3.44882	-1.01204	-0.73846
C	-2.36799	-0.97689	0.167252
C	-1.93753	0.338128	0.743505
C	-3.84855	-2.21043	-1.33164
C	-3.20049	-3.39571	-1.01611
C	-2.14952	-3.38246	-0.10372
C	-1.72114	-2.19339	0.487492
O	-0.86716	0.471159	1.317359
O	-5.13936	0.17325	-1.89486
N	-0.67977	-2.30126	1.460544
C	0.626522	-1.89908	1.376933
C	1.061492	-1.45934	-0.0232
N	2.377611	-0.73771	-0.10104
O	1.377608	-1.97324	2.326385

C	2.403247	0.459718	0.831352
C	3.533249	-1.6642	0.214973
C	2.527151	-0.24477	-1.52242
H	1.135047	-2.34551	-0.65846
H	0.315009	-0.8023	-0.45989
H	-3.14136	4.7227	1.611263
H	-5.06691	4.638554	0.047287
H	-5.55729	2.534306	-1.20141
H	-1.70253	2.715363	1.916179
H	-4.67782	-2.18639	-2.028
H	-3.51209	-4.32927	-1.47122
H	-1.64019	-4.3007	0.167374
H	-0.93305	-2.64107	2.379391
H	2.464489	0.09616	1.8505
H	3.269994	1.060189	0.577908
H	1.478911	1.015078	0.688937
H	3.385895	-2.06088	1.213113
H	3.536002	-2.46283	-0.52681
H	4.452108	-1.09071	0.151518
H	3.520443	0.173029	-1.64636
H	2.384159	-1.08797	-2.19774
H	1.772471	0.519163	-1.70348
B	5.686613	1.179416	-0.58275
F	6.874064	1.851561	-0.74447
F	5.59822	0.048179	-1.45452
F	4.56328	2.013643	-0.86944
F	5.524322	0.695696	0.746569

Coordinates of optimized structures of [AQN]⁺

C	-4.11754	-2.65178	-0.14093
C	-4.96412	-1.7027	0.438855
C	-4.50204	-0.41402	0.67968
C	-3.19481	-0.06074	0.332054
C	-2.34222	-1.0137	-0.24813
C	-2.81133	-2.31162	-0.47494
C	-2.71772	1.320082	0.585931
C	-1.36919	1.696553	0.057638
C	-0.49826	0.738328	-0.51165
C	-0.9275	-0.69053	-0.58772
C	-1.0152	3.043834	0.111052
C	0.193135	3.472427	-0.42451
C	1.058318	2.54739	-0.99374
C	0.737407	1.187532	-1.03016
O	-0.16228	-1.58891	-0.91217
O	-3.41066	2.135407	1.175864

N	1.68277	0.341496	-1.67292
C	2.415688	-0.69258	-1.17482
C	2.30561	-0.97889	0.32307
N	3.573149	-0.62669	1.083558
O	3.17242	-1.33766	-1.88412
C	4.727354	-1.51299	0.696819
C	3.934398	0.81486	0.851761
C	3.282598	-0.83044	2.546904
H	1.510172	-0.41962	0.803357
H	2.130565	-2.04291	0.460667
H	-4.47748	-3.65752	-0.32862
H	-5.98143	-1.97076	0.702416
H	-5.1441	0.331361	1.133589
H	-2.14431	-3.04416	-0.91287
H	-1.70351	3.747627	0.562157
H	0.464335	4.521609	-0.39485
H	2.006641	2.86398	-1.413
H	1.896481	0.568633	-2.63767
H	4.949265	-1.37189	-0.35497
H	5.582133	-1.23634	1.310458
H	4.443748	-2.54648	0.884288
H	4.22256	0.949233	-0.18839
H	3.069453	1.431936	1.085156
H	4.769385	1.067874	1.50076
H	4.186501	-0.6113	3.110639
H	2.481469	-0.15673	2.842344
H	2.983256	-1.86504	2.700506

Supporting References

1. L. Timperman, P. Skowron, A. Boisset, H. Galiano, D. Lemordant, E. Frackowiak, F. Beguin and M. Anouti, *Phys. Chem. Chem. Phys.*, 2012, **14**, 8199-8207.
2. S. J. Schmidtke, D. F. Underwood and D. A. Blank, *J. Phys. Chem. A*, 2005, **109**, 7033-7045.
3. A. J. Bard and L. R. Faulkner, *Electrochemical methods: fundamentals and applications*, Wiley, 2001.
4. M. J. Frisch, G. W. Trucks, H. B. Schlegel and et al., *Gaussian 09, Gaussian, Inc. Wallingford CT*, 2013.
5. T. Lu and F. Chen, *J. Comput. Chem.*, 2012, **33**, 580-592.
6. G. Kwon, S. Lee, J. Hwang, H.-S. Shim, B. Lee, M. H. Lee, Y. Ko, S.-K. Jung, K. Ku, J. Hong and K. Kang, *Joule*, 2018, **2**, 1771-1782.
7. B. Hu and T. L. Liu, *J. Energy Chem.*, 2018, **27**, 1326-1332.
8. J. Huang, Z. Yang, M. Vijayakumar, W. Duan, A. Hollas, B. Pan, W. Wang, X. Wei and L. Zhang, *Adv. Sustainable Syst.*, 2018, **2**, 1700131.
9. G. Kwon, K. Lee, M. H. Lee, B. Lee, S. Lee, S.-K. Jung, K. Ku, J. Kim, S. Y. Park, J. E. Kwon and K. Kang, *Chem*, 2019, **5**, 2642-2656.
10. J. Chai, A. Lashgari, X. Wang, C. K. Williams and J. J. Jiang, *J. Mater. Chem. A*, 2020, **8**, 15715-15724.